On the formation and stability of disks in binaries with intermediate separations

M. Huarte-Espinosa[1], J. Carroll-Nellenback[1], J. Nordhaus[1,2], A. Frank[1] and E. G. Blackman[1]

Received _____; accepted _____

[1]Department of Physics and Astronomy, University of Rochester, 600 Wilson Boulevard, Rochester, NY, 14627-0171

[2]RIT...

ABSTRACT

Subject headings: ? — ? — ? —

1. Introduction

The process of accretion from a primary wind onto a secondary star is a specific case of Bondi-Hoyle-Lyttleton (BHL) accretion (e.g. Edgar 2004 for a review) and is observed to play a direct role in the phenomenology of some asymmetric PPN (the best studied example is the Red Rectangle; Witt et al. 2009). Disk formation around the secondary via AGB wind capture was first studied computationally with SPH calculations 14 years ago (Mastrodemos & Morris 1998), then by Podsiadlowski & Mohamed (2007) using GADGET, and more recent 2D FLASH simulations of BHL accretion were performed by de Val-Borro et al. (2009). These studies found signicant enhancements over BHL accretion rates onto the secondary. Such result however must be tested in 3- D using high resolution simulations because the implications for the maximum outflow (jet) power are dramatic; the answer could rule in, or out, the secondary as the engine powering jets in pot-AGB stars and Young Stellar Objects (YSO).

1.1. Bondi-Hoyle accretion onto a moving object (impact parameter)

The BHL accretion occurs when a compact object of mass, m, moves at a constant supersonic velocity, v_w, though an infinite gas cloud which is homogeneous at infinity. The gravitational field of m focuses the cloud material located within the BHL radius

$$r_b = 2Gm/v_w^2 \tag{1}$$

into a wake. A conical shock is formed and divides the wake into (i) material that is accreted (ii) material that flows away from the object. These flow components are separated by a stagnation point (Bondi & Hoyle, 1944).

Here we study a system in which the cloud material is that of an AGB star's wind,

tens of AU away from the central star, with a terminal speed v_w. The accretor is an orbiting companion of mass, $m = m_s$, which has a constant acceleration that points towards the primary. The wake that develops under these conditions is not aimed towards the instantaneous position of the companion as in the BHL accretion. Instead, the wake aims towards a point between the companion's original and current positions; the focused material is accelerated on average towards a retarded position. The time-scale associated with this wind capture process scales up with r_b/v_w. Thus the distancei, I, that a volume of gas, dv, has moved due to this acceleration is

$$I = (2a_c t^2 \cos\alpha)^{-1}, \tag{2}$$

where α is the angle between $\mathbf{v}_w$ and the acceleration vector. We call I "the impact parameter".

In an inertial reference frame that co-rotates with the secondary at t_0, the companion accelerates towards the primary at $r_s\Omega^2$. The projection of this relative to the incoming flow velocity is then

$$r_s\Omega^2 \frac{v_s}{\sqrt{v_s^2 + v_w^2}}. \tag{3}$$

Given that acceleration of the captured material occurs during a time scale

$$\frac{r_b}{\sqrt{v_s^2 + v_w^2}}, \tag{4}$$

the offset scales up with

$$\frac{v_s^3 r_b^2}{2r_s(v_s^2 + v_w^2)^{3/2}}\hat{\mathbf{r}}. \tag{5}$$

This implies the wake, or "backflow", returns at some small distance from the secondary and will then proceed into a prograde orbit about the secondary. In summary, I falls off with the orbital radius supporting the fact that disks start small.

2. Model

We model the formation and evolution of disks formed in binaries due to wind capture. We solve the equations of hydrodynamics in three-dimensions, which in non-dimensional conservative form are:

$$\frac{\partial \rho}{\partial t} + \nabla \cdot (\rho \mathbf{v}) = 0 \tag{6}$$

$$\frac{\partial \mathbf{v}}{\partial t} + (\mathbf{v} \cdot \nabla)\mathbf{v} = -\frac{1}{\rho}\nabla p - \Phi \tag{7}$$

where ρ, p and $\mathbf{v}$ are the gas density, thermal pressure and flow velocity, respectively. We use an isothermal equation of state, thus $\gamma = 1$. In (7)

$$\Phi = \begin{cases} -\frac{Gm_s}{\sqrt{r}}, & \text{for } r > 4dr; \\ -\frac{Gm_s}{\sqrt{4_{dr}}}, & \text{for } r \leq 4dr. \end{cases} \tag{8}$$

where $4dr = 4\sqrt{dx^2 + dy^2 + dz^2}$ is the softening radius.

We solve these equations using the adaptive mesh refinement (AMR) numerical code *AstroBEAR2.0*[1] which uses a single step, second-order accurate, shock capturing scheme (Cunningham et al. 2009; Carroll-Nellenback et al. 2011). While AstroBEAR2.0 is able to compute several microphysical processes such as gas self-gravity and heat conduction, these are not considered in the present study.

[1]https://clover.pas.rochester.edu/trac/astrobear/wiki

2.1. Grid and facilities

We use a box-like computational domain with a volume of 10x10x5 AU^3 and a fixed grid with 64x64x32 base cells plus four levels of refinement. Nested cell blocks were centered at the secondary's position, and the innermost block had 32-64 finest cells (on the orbital plane) to resolve the central part of the disks.

We use either wind boundary conditions (section 2.2.3) in the $-x, +y$ and $\pm z$ domain faces, or outflow only conditions in all other faces (Figure 1). The positions of the primary, the center of mass and the secondary are ($-r_p$,0,0), (0,0,0) and (r_s,0,0), respectively. We use a reference frame which co-rotates with the secondary, thus Coriolis terms are included in (7).

We use *BlueHive*[2] –an IBM massively parallel processing supercomputer of the Center for Integrated Research Computing of the University of Rochester– and *Ranger*[3] –a Sun Constellation Linux Cluster which is part of the TeraGrid project– to run simulations for an average running time of about
?
day/orbit using 64–512 processors.

2.2. Initial conditions

We are interested in binaries formed by an AGB primary and a main sequence, or white dwarf, companion.

[2]https://www.rochester.edu/its/web/wiki/crc/index.php/ Systems#Blue_Gene.2FP

[3]https://www.xsede.org/web/guest/tacc-ranger

2.2.1. Primary

We use a simple AGB star model for the primary. It consists of a mass of $1.5\,M_\odot$ and a wind/circumstellar ambient medium with an isotropic velocity of $v_w = 10\,\mathrm{km\,s^{-1}}$ and a mass-loss rate of $\dot{m}_p = 10^{-5}\,M_\odot\,\mathrm{yr}^{-1}$. These values are based on representative observations of AGB stars (e.g. Hrivnak et al. 1989; Bujarrabal et al. 2001).

We note two aspects of this model. First, winds off AGBs seem to be formed by a highly non-linear interaction between radiation pressure and dust grains. Observations and models (e.g. see Sandin 2008, and references therein) suggest that AGB winds have a radial acceleration profile which monotonically decreases with distance form the central star. Such acceleration region may play a role in the formation of disks in binaries with separations $\lesssim 10\,\mathrm{AU}$. We expect this effect to be mild for the separations explored here (10-20 AU), thus no acceleration region has been considered. We leave more realistic AGB star wind models for future work. Second, the binary separations that we explore here are either not far in the 10 AU case or far in the 20 AU one, from the WRLOF limit (Sandin 2008; Mohamed & Podsiadlowski 2011).

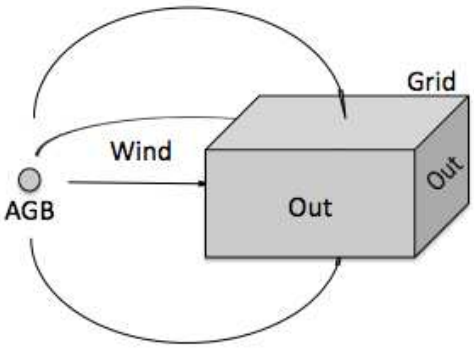

Fig. 1.— Model diagram.

2.2.2. Companion

We model the secondary star using a sink particle, based on the implementation of (Federrath et al. 2010), which accretes gas within a radius of 4 grid cells. The mass, momentum and energy of the gas within this region is then acquired by the particle in a conservative fashion. We set the particle with an initial mass of $1\,\mathrm{M}_\odot$ in a circular orbit about the primary.

2.2.3. Wind solution

We set the initial conditions throughout the grid with a constant temperature of 1000 K and a density given by

$$\rho_w = \frac{\dot{m}_p}{4\pi(\mathbf{x}_p - \mathbf{x})^2 v_w}, \tag{9}$$

where $\dot{m}_p = 5\times 10^{-5}\,\mathrm{M}_\odot\,\mathrm{yr}^{-1}$, $v_w = 10\,\mathrm{km\,s}^{-1}$, $\mathbf{x}_p$ and $\mathbf{x}$ are the positions of primary's orbit and that of an arbitrary grid cell relative to the centrer of mass (0,0,0), respectively. We calculate the velocity field of the solution by solving for the characteristics that leave the surface of the primary at a *retarded* time, $t_r = t - |\mathbf{x}|/v_w$, with a velocity vector pointing towards $\mathbf{x}$. Wind speeds are chosen so that $v_w > |\mathbf{v}_s|$, where $\mathbf{v}_s$ is the secondary's orbital velocity. We assume that the distance from the primary's surface to $\mathbf{x}$ is larger than $|\mathbf{x}_p|$, which constraints the separation between the secondary and the grid's boundaries. As time goes from t_r to t, the primary covers a circular segment of radius r_p starting at $\mathbf{x}_p(t_r)$, with a displacement vector $\mathbf{d} = \mathbf{x} - \mathbf{x}_p(t_r)$. We calculate the wind normal, $\hat{\mathbf{n}}$, so that $(v_w\hat{\mathbf{n}} + \mathbf{v}_p(t_r)) \times \mathbf{d} = 0$. Starting at the primary's surface, the wind velocity is then

$$\mathbf{v}_w = v_w\hat{\mathbf{n}} + \mathbf{V}_p(t_r), \tag{10}$$

which yields a better approximation of the retarded time

$$\tau_r = t - |\mathbf{x}|/|\mathbf{v}|. \tag{11}$$

We iterate the above computations until we find a convergent wind solution for the gird cell located at $\mathbf{x}$. Finally, we transform the solution to a reference frame which co-rotates with the secondary.

2.3. Wind injection

We continually set the above wind solution at grid cells in the $-x, +y$ and $\pm z$ domain faces. For each iteration however we use τ, $\mathbf{x}_p(\tau)$ and $\mathbf{v}$ as initial conditions in a recursive Runge-Kutta method to calculate the deflection of $\mathbf{v}$, as it travels from the primary's surface ($\sim\ x_p(\tau)$) to $\mathbf{x}$, caused by the secondary's gravity field. We consider the orbital motion of the secondary in these computations. This step yields yet better estimates of both $\hat{\mathbf{n}}$ and τ than the calculations in section 2.2.3 alone. We therefore use the new values of $\hat{\mathbf{n}}$ and τ for the next iteration of the wind solution (above).

Finally, to match the initial conditions and the injected wind solution we allow the gravitational effect that the secondary had on the gas to increase linearly during one wind crossing time, $1.6r_b/v_w$, from zero to Gm_s/r. The field remains constant thereafter. This has no effect on the binary orbital motion.

2.4. Simulations

We carry out three simulations corresponding to stellar separation of 10, 15 and 20 AU. All the other parameters are fixed.

3. Results

3.1. Disk structure and formation

In Figure 2 we show logarithmic density contours of the disk on slices though the orbital plane (face-on; left panels) and though a longitudinal plane (edge-on; right panels) aligned with the wind's inflow direction. Each panel has 12 contours arranged by line type and color: blue, red and black represent densities of 3.5, 10.5 and $35\times10^{10}\,\mathrm{part\,cm^{-3}}$, respectively. Dashed, dotted and dashed-dotted lines represent densities at $t=1$, 2 and 3 orbits, respectively.

The density contour maps are very consistent and show a clear dependence of disk properties with a. Comparing same color lines (Figure 2) we see that the structure of the disks changes only mildly after their formation. Our model disks are thin, not symmetric and have a flared vertical structure. We find the steepest density gradients located where the disks face the incoming wind (top left region in left panels and left region in right panels), and that both the disks' radius, r_d, and edge height are inversely proportional to a. In section 4.1 we show that the shape of the disk gas orbits is a function of a as well.

Comparing the solid lies in left panels we find, in agreement with the discussion in section 1.1, that the angle between the flow that directly accretes onto the particle and the wind decreases with a. This angle is close to zero already in the 20 AU model. Thus the solution (5) converges to the BHL one for large separations.

In addition to disk density contour maps (above), in Figure 3 we present logarithmic density gray-scale and velocity field maps at $t=2$ orbits. Rows 1 and 2 show slices though the orbital plane, while the bottom row shows slices though longitudinal planes which are aligned with the winds' inflow direction.

Firstly, we see that the large scale structure of the flows is quite similar for both a

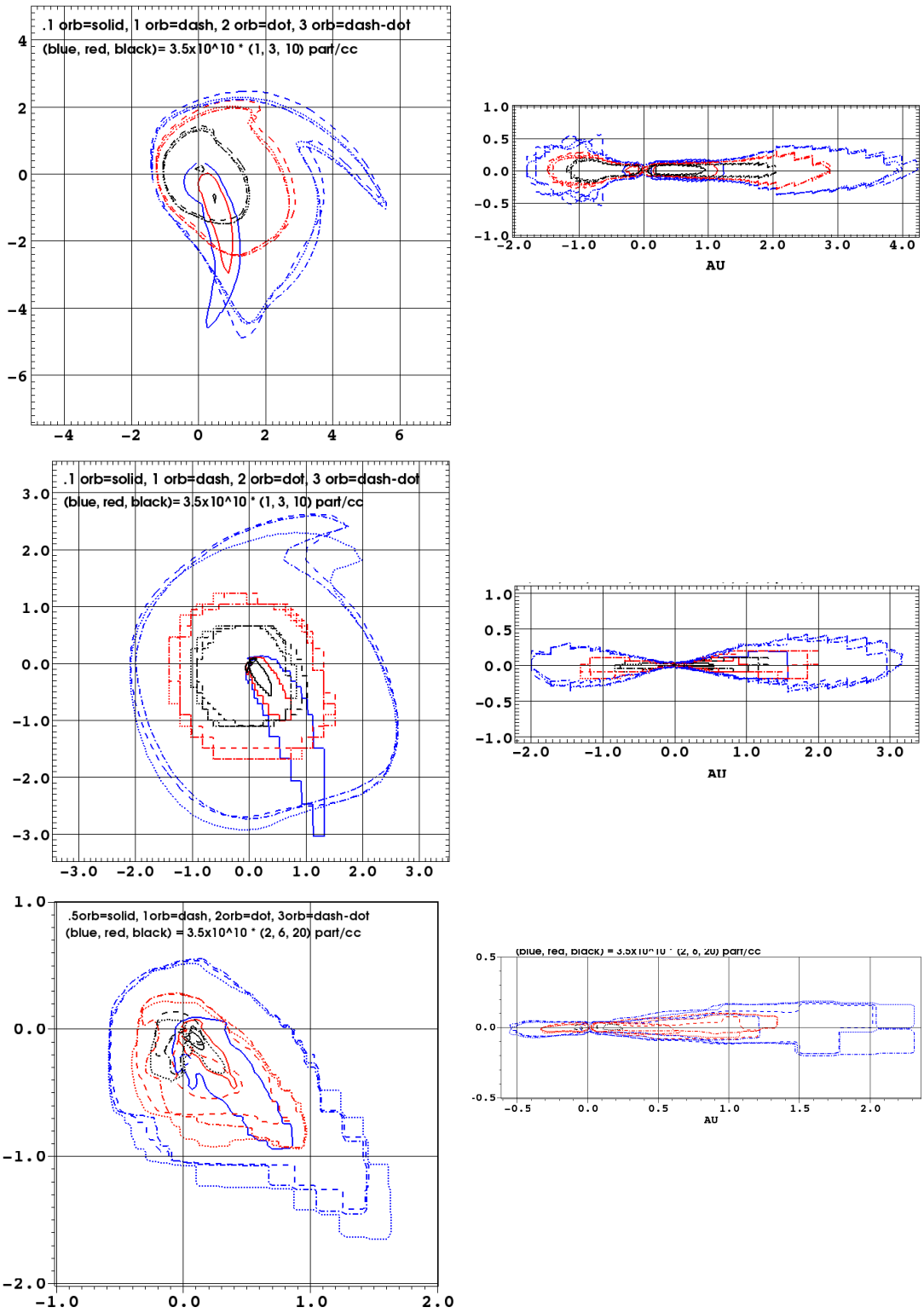

Fig. 2.— Disk density structure at 4 times. Left: face-on view. Right: edge-on view. Top, middle and bottom rows correspond to binary separations of 10, 15 and 20 AU, respectively.

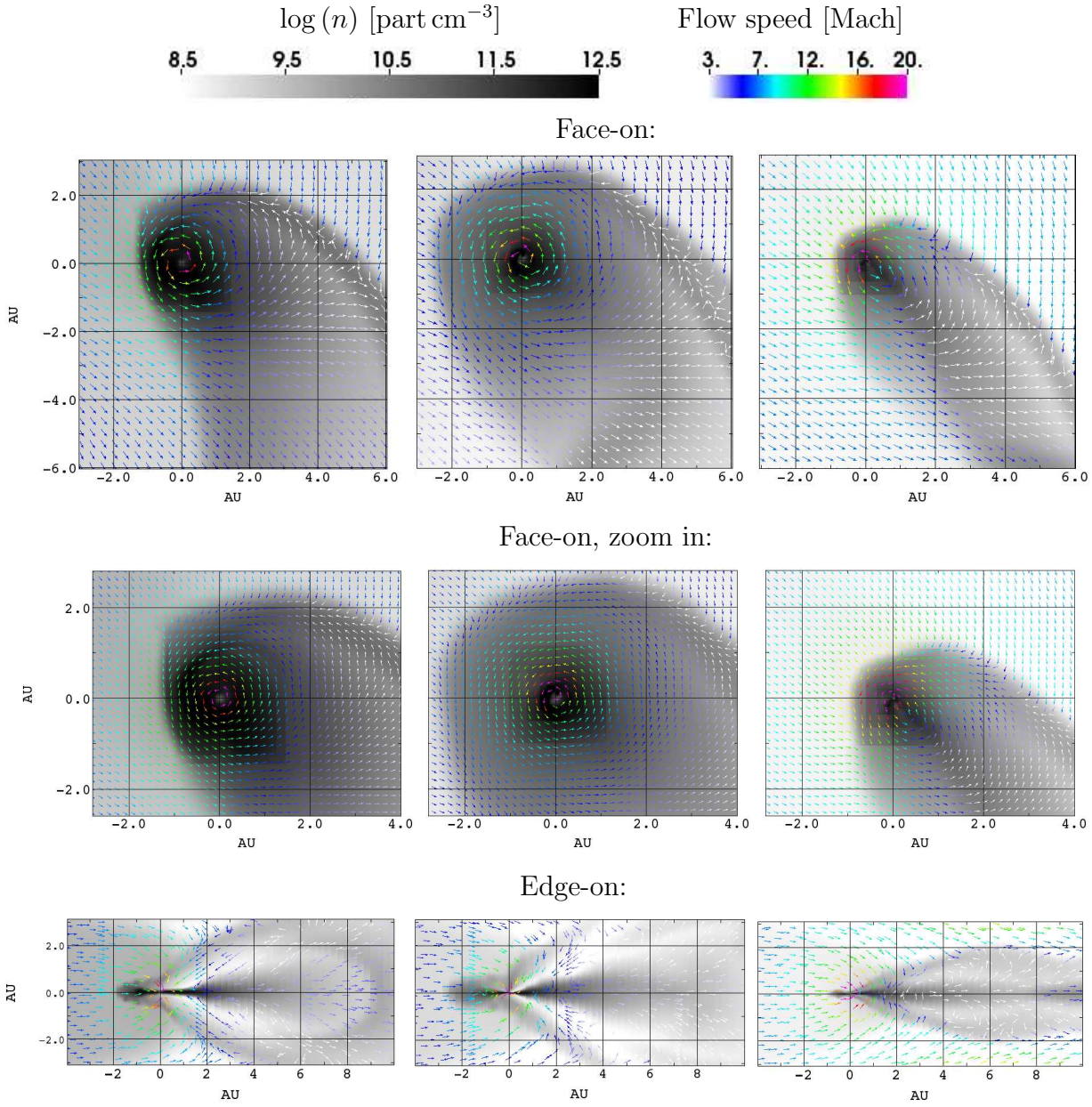

Fig. 3.— Logarithmic density gray-scale and velocity field maps for the 10 AU (left), 15 AU (middle) and 20 AU (right) models at $t = 2$ orbits.

cases. The top and bottom panels show that the disks drive characteristic bow shocks on the ambient medium. This is the first time that such structures have been resolved and followed in 3-D binary-formed disks numerical simulations. These bow shocks are formed by the interaction between the disks' gas, the AGB winds' gas which has been deflected by the secondary and the incoming AGB winds' gas. Located between the secondary and the bow shocks, we find accretion wakes. In both a cases, the volume of the wake increases about 64-fold in a matter of $\sim .5$ orbits. The ram pressure of the defected gas scales down with a because of the binaries' orbital motion. For this reason we see that the volume of the wakes also decreases with increasing a (compare left to right panels). We note however that this effect is moderately affected by the grid resolution that we use about the secondary; the higher the resolution the deeper we resolve the secondary's gravitational potential. e.g. an additional 10 AU test simulation was carried out (not shown) and revealed that the area extended by the wakes on the orbital plane is $\sim 1\,\mathrm{AU}^2$ larger when using 4 AMR levels than when using 2.

3.2. Disk mass

In Figure 4 we show profiles of the disks' mass (solid lines) as a function of time and binary separation. These are calculated by adding the mass of grid cells which contain bound gas (the gravitational energy is greater than the kinetic one).

In the 10 AU case we see that the mass increases during the first 1.5 orbits and reaches a maximum value of $1.1\times10^{-5}\,\mathrm{M}_\odot$. The profile then oscillates with a wavelength of $\sim$1 orbit and an amplitude of about $3\times10^{-6}\,\mathrm{M}_\odot$. The oscillations seem to be damped in time.

To understand the origin of the disk mass oscillations we have also calculated the flux

of gas that leaves the grid though the $+x$ and $-y$ boundaries in $M_\odot\,yr^{-1}$ (dashed line; Figure 1). The position and shape of the gradients in the solid and dashed lines show that the disk's mass decreases when the flux of gas away form the grid increases, and viceversa. This suggests that the wind's ram pressure is able to strip a small yet significant fraction of disk's gas.

The disk mass profiles of the 15 AU model is similar to the 10 AU one, but the former reaches its maximum value of about $4\times 10^{-6}\,M_\odot$ in ~ 0.7 orbits (earlier). We see disk mass oscillations centered at $3.5\times 10^{-6}\,M_\odot$ due to wind stripping (dashed profiles), with an amplitudes of about $1\times 10^{-6}\,M_\odot$and a frequency of ~ 0.3 orbits. These oscillations are smaller and faster than in the 10 AU case. This is because the wind's ram pressure is proportional to $a^{-2}\,\mathbf{x}_s^{-1}$, where $\mathbf{x}_s^{-1}$ is the distance between the secondary and the center of mass.

The disk mass profile of the 20 AU model is quite different. We see some initial mass which corresponding to gas that accretes onto the particle. The disk forms at $t \approx 0.85$ orbits. The disk's mass increases very fast then, in a matter of 5.5 yr, and reaches a maximum value of $\sim 6.5\times 10^{-7}\,M_\odot$. Next, after a brief relaxation period, the disk mass profile converges to $\sim 6.5\times 10^{-7}\,M_\odot$. We do not see any disk mass oscillations related to wind stripping as in the other models; the wind ram pressure is the weakest in the 20 AU case.

3.3. Accretion onto the companion

In Figure 5 we show the evolution of the sink particle's accretion rate. The profiles represent the amount of gas that flows into a region within a 4 cell radius from the particle's center (section 2.2.2) as a function of time. The plots consistently show a very steep initial increase which lasts for about 0.1 orbits and then they oscillate mildly with a frequency

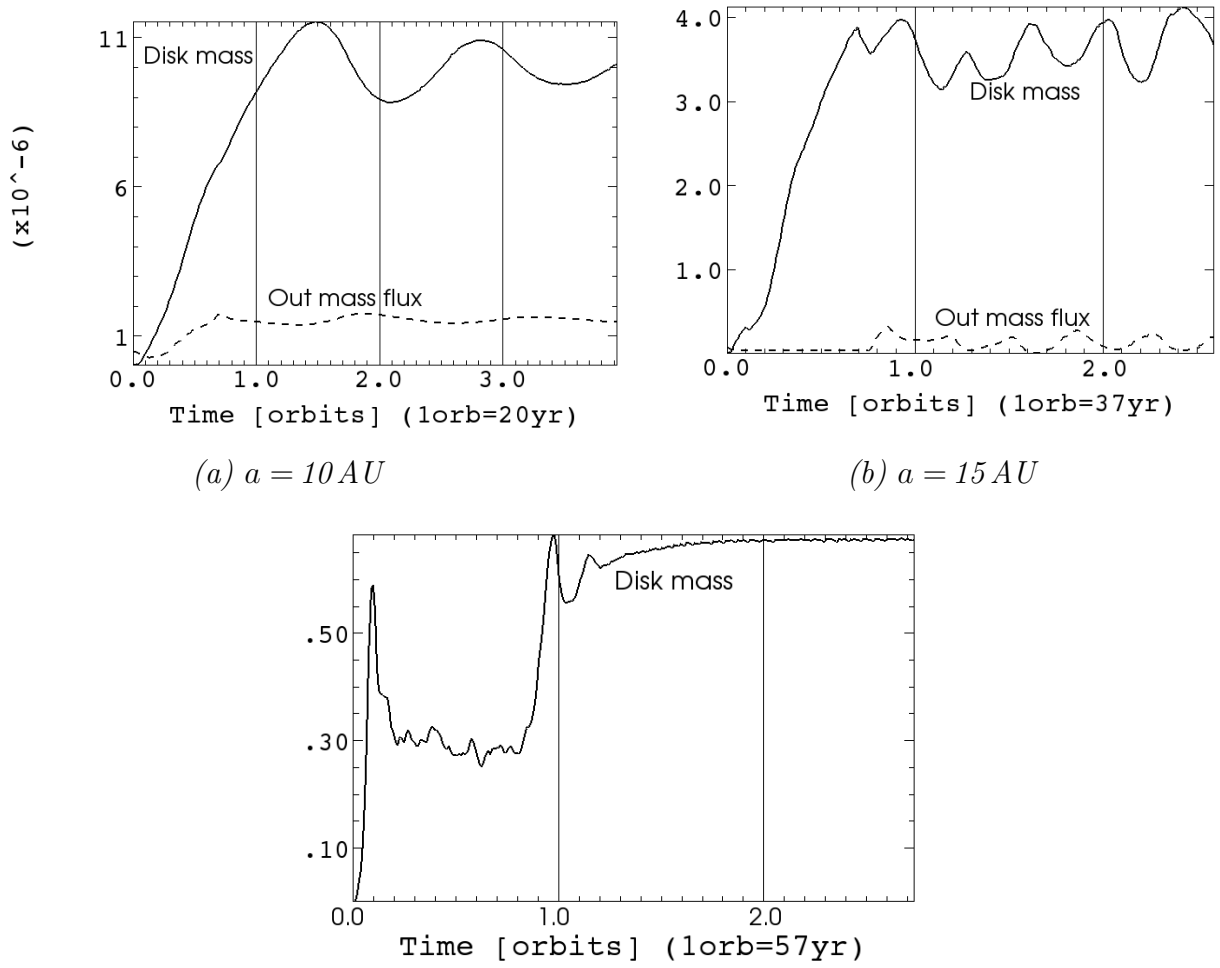

(a) $a = 10\,AU$

(b) $a = 15\,AU$

(c) $a = 20\,AU$

Fig. 4.— Disk mass as a function of time [$M_\odot$] (solid) and flux of gas that leaves the grid [$M_\odot\,yr^{-1}$] (dashed).

that decreases with a. These gradients are consistent with those found in the accretion rate profiles of de Val-Borro et al. (2009, see their figure 12). We see a small dip in the 20 AU profile, close to 0.9 orbits, which corresponds to the disk formation time.

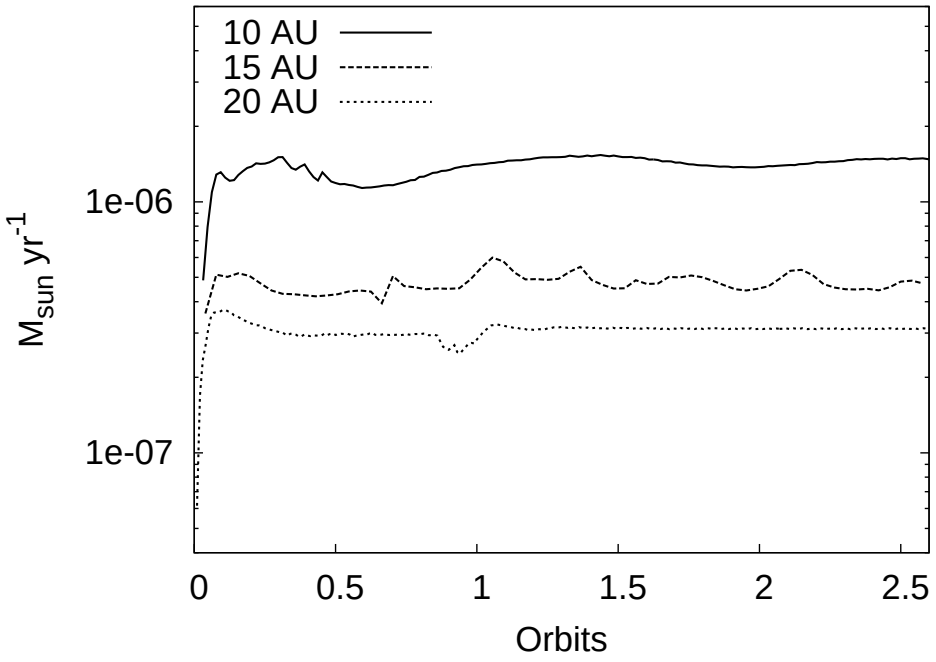

Fig. 5.— Secondary (particle) accretion rate evolution.

The analytic Bondi-Hoyle accretion rate for a high velocity wind and negligible pressure conditions is given by

$$\dot{m}_{BH} = \pi R_b^2 \rho(\mathbf{x}_s) \sqrt{v_w^2 + v_s^2}, \tag{12}$$

where $R_b = 2Gm_s\,(v_w^2 + v_s^2)^{-1}$ is the modified BHL radius (Edgar, 2004). For our 10, 15 and 20 AU models, $\dot{m}_{BH}$ takes the values of 3.3, 1.8 and $1.2\times 10^{-6}\,\mathrm{M}_\odot\,\mathrm{yr}^{-1}$, respectively. Thus the secondary accretion rates we find (Figure 5) are $\dot{m}_{10AU} \sim 0.5\dot{m}_{BH}$, $\dot{m}_{15AU} \sim 0.2\dot{m}_{BH}$, $\dot{m}_{20AU} \sim 0.16\dot{m}_{BH}$.

Comparing with the models of de Val-Borro et al. (2009), we get higher accretion rates. E.g. de Val-Borro et al. (2009, see their table 3) report $\dot{M}_{acc}/\dot{M}_{wind}$ ∼0.06 after 2 orbits

for a 70 AU case. We expected higher accretion rates in our 3D simulations than in their 2D ones, since only ours capture poloidal accretion. On the other hand, the semi-analytic models of Perets & Kenyon (2012) yield $\dot{m}$ values consistent with ours. A clear comparison of our results and those of Perets & Kenyon (2012) is difficult because the models are quite different. In particular, Perets & Kenyon (2012) explore disk evolution for time periods four orders of magnitude larger than we do.

THE FOLLOWING NEED EXTENSION: Our models are quite relevant for common envelope evolution binaries which have conditions to eject poloidal outflows, or jets, from a magnetized accretion disks around a white dwarf companion. Blackman & Nordhaus (2007) have estimated jet mass losses for post-AGB stars of order $5\times 10^{-4}\,\mathrm{M}_{\odot}\,\mathrm{yr}^{-1}$. The accretion rates we find in our models are thus insufficient to account for the ejected material in such jets. We note however that a parameter survey -covering a systematic range of: grid resolution setups; accreting radii about the sink particle; gravity softening radii- is very important for future work in this direction, both to understand the connection between core accretion and jet launch in binary-formed disks and to clearly characterise numerical artifacts.

4. Discussion

4.1. Disk orbits

An interesting result from our simulations is that the shape and stability of the disk gas orbits strongly depend on a. To show this relation we present disk gas streamlines in Figure 6, where the top panel depicts a 3-D map of the disk gas velocity distribution for the 10 AU model, along with sliced density contours in translucent red color. The lines show that the gas is supersonic, the orbits have low eccentricities and the velocity decreases with

r_d

In the bottom panel of Figure 6 we show a quantitative comparison of disk gas orbits as a function of a (black vs. red) and time (thin vs. thick lines). We see that

the eccentricity scales down with a

gas in the 10 AU disk has stable orbits while gas in the 20 AU diks orbits 3 or 4 times about the secondary in highly eccentric orbits and is the accreted.

$\epsilon \propto a^{\beta}$.

4.2. Grid resolution

Accretion disk simulations are known to be affected by grid resolution. To assess this matter we have carried out additional runs of our simulations (see Table 1) but with slight resolution variations. For the 10 AU case we independently tried (1) a lower grid resolution of 64^3 cells (four times smaller that in Model 1) and (2) increasing the volume of the central box of finest cells around the particle (section 2.2) from $(r_b/4)^3$ (Model 1) to $(r_b/2)^3$. Only the small scale features of the disks show differences.

5. CONCLUSIONS AND SUMMARY

Wind ram pressure is able to strip disk material in an oscillatory fashion for $a < 20$ AU. The effect scales with $a^{-2}\,\mathbf{x}_s^{-1}$.

Financial support for this project was provided by the Space Telescope Science Institute grants HST-AR-11251.01-A and HST-AR-12128.01-A; by the National Science Foundation under award AST-0807363; by the Department of Energy under award DE-SC0001063;

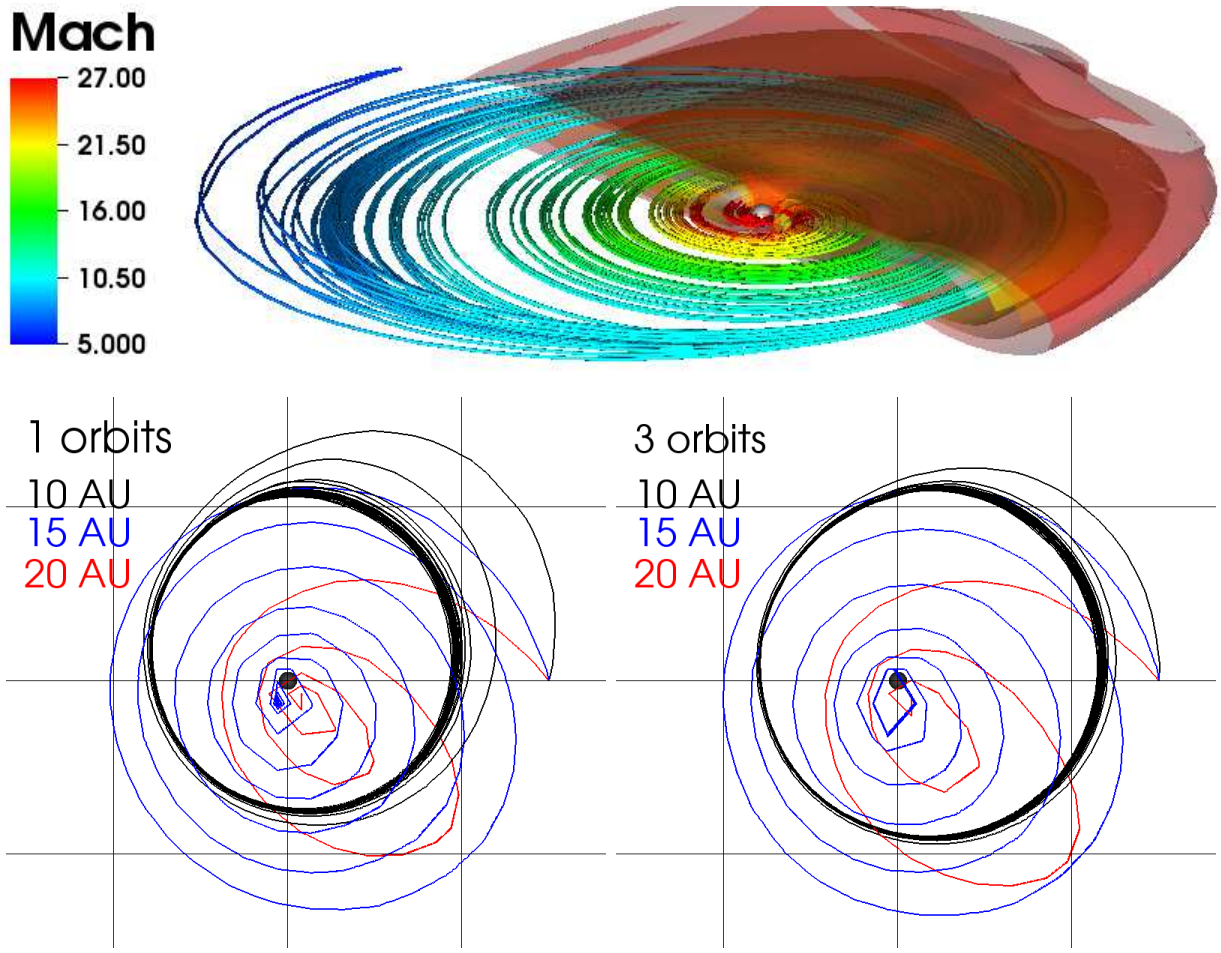

Fig. 6.— Top: 3-D disk gas orbit streamlines and sliced density contours (red) for the 10 AU case at $t = 2$ orbits. The central white small sphere is the secondary's particle. Streamline colors denote orbital speed in Mach units. The wind enters the grid towards the image. Bottom: Disk gas orbit streamlines comparison on the binary orbital plane. Grid squares are 1 AU^2. The wind enters the grid from the top left corner towards the bottom right.

and by Cornell University grant 41843-7012. This work used the Extreme Science and Engineering Discovery Environment (XSEDE), which is supported by National Science Foundation grant number OCI-1053575.

REFERENCES

Blackman, E. G., Frank, A., & Welch, C. 2001, ApJ, 546, 288

Blackman, E. G., & Nordhaus, J. T. 2007, Asymmetrical Planetary Nebulae IV

Blackman E.G., 2007, Ap&SS, 307, 7

Blandford, R. D., & Payne, D. G. 1982, MNRAS, 199, 883

Bujarrabal, V., Castro-Carrizo, A., Alcolea, J., Sánchez Contreras, C., 2001, AAP, 377, 868

Carroll-Nellenback, J. J., Shroyer, B., Frank, A., & Ding, C., 2011, arXiv:1112.1710

Cunningham A. J., Frank A., Varnière P., Mitran S., & Jones, T. W. 2009, ApJS, 182, 519

Edgar, R., 2004, New A Rev., 48, 843

Federrath, C., Banerjee, R., Clark, P. C., & Klessen, R. S., 2010, ApJ, 713, 269

Hrivak, B. J., Kwok, S., Volk, K. M., 1989, ApJ, 346,265

Mastrodemos, N., & Morris, M., 1998, ApJ, 497, 303

Makita, M., Miyawaki, K., & Matsuda, T., 2000, MNRAS, 316, 906

Mohamed, S., & Podsiadlowski, P., 2007, Asymmetrical Planetary Nebulae IV

Mohamed, S., & Podsiadlowski, P., 2011, Why Galaxies Care about AGB Stars II: Shining Examples and Common Inhabitants, 445, 355

Perets, H. B., & Kenyon, S. J., 2012, arXiv:1203.2918

Sandin, C. 2008, MNRAS, 385, 215

Soker, N., & Rappaport, S., 2000, ApJ, 538, 241

de Val-Borro, M., Karovska, M., & Sasselov, D., 2009, ApJ, 700, 1148

Witt, A. N., Vijh, U. P., Hobbs, L. M., et al., 2009, ApJ, 693, 1946

This manuscript was prepared with the AAS LaTeX macros v5.2.